KSCE Journal of Civil Engineering (2022) 26(1):460-471
DOI 10.1007/s12205-021-5929-y

pISSN 1226-7988, eISSN 1976-3808
www.springer.com/12205

Tunnel Engineering

Progressive Failure Process of Anisotropic Rock: Insight from Full-Field Strain Evolution

Yangyi Zhou[a], **Xufeng Liu**[a], **and Xifan Li**[a]

[a]*Key Laboratory of Ministry of Education on Safe Mining of Deep Metal Mines, Northeastern University, Shenyang 110819, China*

ARTICLE HISTORY

Received 22 May 2021
Revised 7 July 2021
Accepted 26 July 2021
Published Online 14 September 2021

KEYWORDS

Anisotropic rock
Full-field strain
Progressive failure process
Digital image correlation

ABSTRACT

Rocks with layered structure (bedding or foliation) usually exhibit different levels of anisotropy in terms of mechanical properties. The structural anisotropy has pronounced influence on the failure process of anisotropic rock. However, relatively few studies have been carried out on the subject. In this paper, the failure processes of a foliated gneiss with different schistosity orientations under uniaxial compression were studied based on digital speckle correlation method. The results show that the evolution process of full- field strain of the gneiss is closely related to the schistosity orientation. More specifically, when $\beta = 0°$, the strain concentration zone mainly originates from the microstructure, and the potential failure plane cannot be observed before total failure. When $\beta = 30°$ or $60°$, there are several strain concentration strips before failure. The ultimate failure is due to the interaction among these strips under the action of local stress field. When $\beta = 90°$, the initiation and evolution of strain concentration strip is relatively stable. When tensile failure occurs along the schistosity, the crack opens abruptly during loading. In contrast, the crack presents a gently stable growth trend, when the shear failure occurs along the schistosity.

1. Introduction

Rocks with layered structure, such as most sedimentary rocks and several metamorphic rocks, constitute the majority of rocks in nature. Different from the nearly isotropic rocks, the layered rocks have dominant orientation in material composition or internal structure (Li et al., 2018). Various discontinuous planar structures are formed, such as bedding, foliation, schistosity, cleavage, etc. Due to the existence of layered structure, the directional dependence of mechanical properties for layered rocks is considerably common. During the excavation of underground openings in layered rock mass, various failure modes will appear in the surrounding rock, such as opening and sliding along bedding (Xu et al., 2015; Chen et al., 2020). The failure phenomena of layered rock mass induced by engineering activities are closely related to the anisotropy of the mechanical behavior originated from layered structure. Therefore, it is particularly important to fully understand the failure process of layered rock with respect to different loading orientations. Conventional loading method, such as uniaxial, conventional triaxial compression and Brazilian splitting tests, etc., are commonly used to study the influence of loading angle β, which is defined as the angle between the normal of bedding and maximum principal stress, on the deformation and failure of layered rocks. Early efforts in this field include Jaeger (1960), Donath (1961), Chenevert and Gatlin (1965) etc. Several decades thereafter, many kinds of rocks, such as slate, schist, and shale, were studied extensively (Nasseri et al., 2003; Zhang et al., 2011; Xiong et al., 2014; Heng et al., 2015). However, these studies only focus on the equivalent mechanical parameters, stress-strain relationships, failure modes, etc., of layered rocks at macroscopic level. Detailed failure process, i.e., the evolution characteristic of strain localization of anisotropic rock is still unclear. Macroscopic failure of rocks is a progressive process involving damage accumulation, crack interaction until ultimate failure (Nicksiar and Martin, 2012), and the damage evolution process of crack has been deeply studied by different numerical simulation methods (Rabczuk and Belytschko, 2004, 2007; Areias et al., 2018; Pan et al., 2019; Ren et al., 2019; Yin et al., 2019). The existence of oriented structures will make this process more complicated. Therefore, a

CORRESPONDENCE Xufeng Liu lxfbym@163.com Key Laboratory of Ministry of Education on Safe Mining of Deep Metal Mines, Northeastern University, Shenyang 110819, China

thorough investigation on the failure process of anisotropic rocks is necessary. The digital speckle correlation method (DSCM), which is a non-contact optical measurement method, has been widely applied to measure the displacement and strain both in and out of plane because of simple equipment and data processing, high accuracy and full-field measurement (Pan et al., 2009). Many studies on the mechanism of crack nucleation, propagation and coalescing of sandstone, granite and limestone specimens have been carried out using DSCM (Dautriat et al., 2011; Song et al., 2013; Yang et al., 2015). However, studies on the non-uniform evolution of strain field of layered rocks at different loading angles are seldom reported.

A series of tests have been conducted on foliated gneiss specimens at different loading angles to investigate the evolution characteristics of full-field strain during failure process by DSCM. Firstly, thin plate specimens with different loading angles (β) are prepared; next, the surface images during loading are captured continuously by a high-resolution CCD camera; finally, the captured images are analyzed by professional software to generate the corresponding full-field strain at different loading stages. Furthermore the difference of strain field evolution between foliated gneiss and nearly isotropic marble, and the identification method of characteristic stress in progressive failure process are also discussed in detail.

2. Material and Testing Methods

2.1 Material Information and Specimen Preparation

The gneiss in this study was sampled from a deep mine. Thin-section observations under cross-polarized light microscope were conducted to identify mineral composition and structure within the gneiss (Fig. 1). According to the identification, the mineral composition of the gneiss mainly includes quartz (~40%), calcite (~30%), muscovite (~25%) and pyrite (~5%). The gneiss shows a scaly granular fine-grained metamorphic structure. The muscovite minerals were fully-cleavage and arranged in a scaly, oriented manner, forming weak planes in the samples, as shown in the dotted box in Fig. 1.

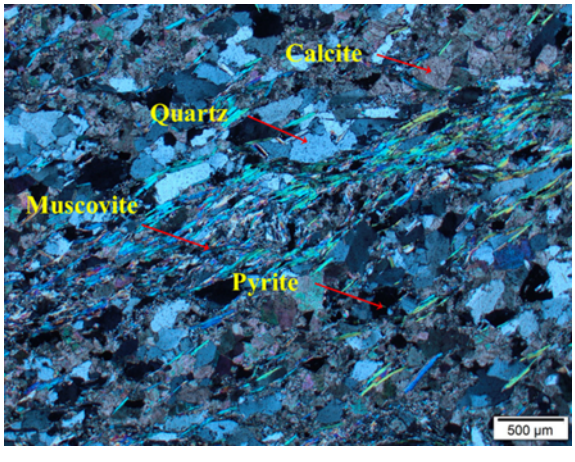

Fig. 1. Polarized Microscopic Image of the Gneiss

Because the mechanical behavior of gneiss is significantly influenced by the schistosity, it is easy to damage and disintegrate along the schistosity under the external disturbance, so the specimen preparation becomes more difficult. Moreover, the mineral composition and structure of most layered rocks (such as gneiss, schist and phyllite etc.) vary greatly with location, which inevitably increases the dispersion of the test results. In the process of investigating the basic mechanical properties of rocks, it is important to reduce the fluctuation of data caused by external factors and increase the repeatability of experimental results (Mogi, 2006). Therefore, specimens should be selected in a smaller area and prepare small-sized rock specimens. Considering the field of view and accuracy of CCD camera, the size of specimen used in this test is 40 mm × 20 mm × 5 mm. This size is believed to be able to realize a quasi-two-dimensional stress condition. To reduce the data fluctuation caused by external factors, a set of preparation method for small-sized thin plate specimens of layered rock is developed. The method entailed the following steps (Fig. 2): the first step was to drill and cut the cylindrical rock samples. More specifically, a cylindrical sample with a diameter of 50 mm was drilled parallel to the schistosity direction, and then the cylindrical sample was cut into a number of cylindrical samples with a thickness of 30 mm (Fig. 2(a)); the second step was to cut the thin plate specimens. More specifically, on the surface of the cylindrical sample, the cutting line was drawn according to the loading angle β and specimen size (Fig. 2(b)), and then the cylindrical sample was cut into a cuboid sample along the cutting line (Fig. 2(c)), then, the cuboid sample was cut into several thin plate specimens (Fig. 2(d)); the third step was grinding. More specifically, the thin plate specimens was fixed in a special fixture, and then polished by a grinder until the specimen size meet the requirements (Fig. 2(e)). The equipment used in specimen preparation is shown in Fig. 3. To obtain better test results, artificial speckle pattern should be made on the

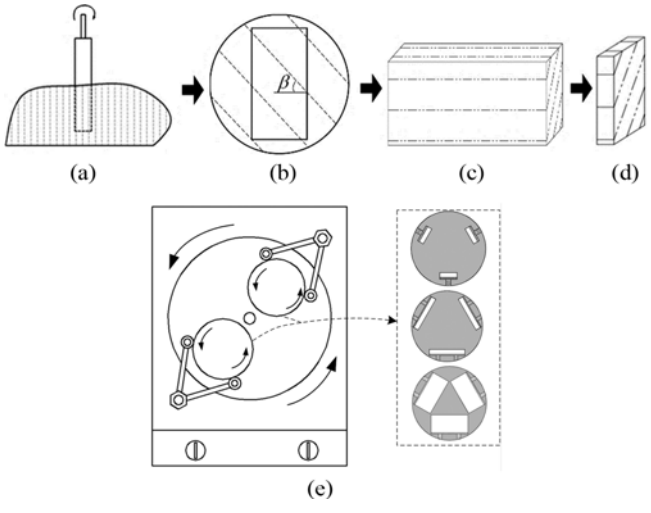

Fig. 2. Schematic Diagram of Specimen Preparation Process: (a) Drill Cylindrical Sample, (b) Mark Cutting Line, (c) Cut into Cuboid Sample, (d) Cut into Thin Plate Specimen, (e) Polish

(a) (b) (c)

Fig. 3. Main Equipment Used in Specimen Preparation: (a) Drilling Machine, (b) Wire Cutting Machine, (c) Grinder

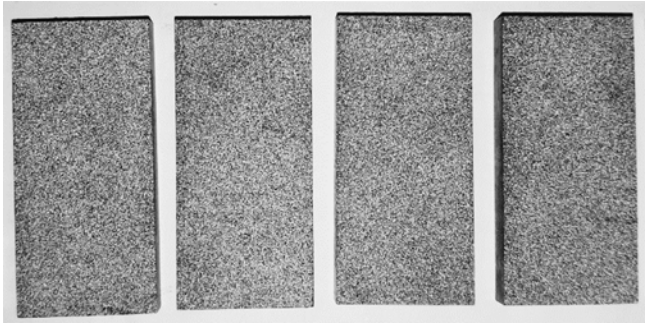

Fig. 4. Specimens with Artificial Speckle Pattern

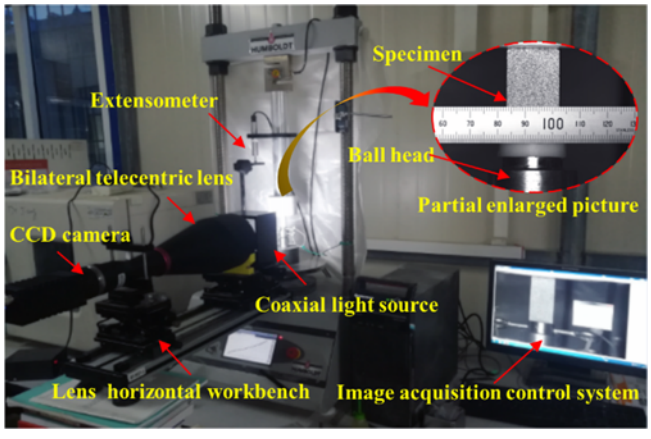

Fig. 5. Test System Setup

surface of the specimen. More specifically, a white matte paint was firstly sprayed evenly on the surface of the specimen, and then after the paint was dry, the black matte paint was sprayed evenly on the surface of the specimen to obtain better contrast effect, as shown in Fig. 4.

2.2 Test Equipment

The testing apparatuses mainly include uniaxial loading system and digital image acquisition system, as shown in Fig. 5. The uniaxial loading system adopts HUMBOLDT 5,030 electronic servo material testing machine, whose maximum loading capacity is 50 kN. The loading mode of the equipment can be controlled by displacement rate or force rate. The digital image acquisition system mainly consists of a high-resolution CCD camera, a bilateral telecentric lens, a coaxial light source and a lens horizontal workbench. The CCD camera has a maximum resolution of 4,896 × 3,264 pixels (roughly 16 megapixels), a maximum 5 frames per second, and a maximum pixel of 5.5 μm. The bilateral telecentric lens has a magnification of 0.38, an object distance of 263 mm, an aperture of 16, very low telecentricity and distortion. The main feature of this lens is that the magnification does not change in the range of depth of field, which reduces the error caused by deformation along the thickness direction. The coaxial light source has 100 × 100 mm^2 emission area and high brightness, providing uniform coaxial lighting. To adjust the position of the camera accurately and ensure good shooting effect, a lens horizontal workbench is designed and made. The workbench allows the lens to be fixed horizontally. The relative position between the lens and the specimen is precisely adjusted by the lifting platform and the linear guide. The size of the specimen is relatively small. If the specimen is unable to be accurately aligned with the loading center during loading, local stress concentration will occur and result in local failure at the end, which can't reflect the true deformation and fracture characteristics of the specimen. Therefore, the self-aligning ball head and positioning cover which are slightly larger than the specimen size are designed, and the copper foil with antifriction agent is padded on the end of the specimen. Thereby, the above problems can be well avoided.

2.3 Testing Procedure

Before the test, the specimen was placed on the ball head and centered by means of the positioning device. Then the brightness of the light source was adjusted to obtain the optimal and stable illumination. During the test, the loading rate was 0.02 mm/min, which was controlled by negative feedback of axial displacement. The image acquisition system ran while loading, and the acquisition rate was 1 frame per second. After the test, the VIC-2D software authorized by the Correlated Solutions, Inc was used to analyze and post-process the collected images. The DIC algorithm adopted in the software was gray value interpolation with 8-tap

splines. The matching criterion was normalized squared differences, and the strain noise-floor was 10 μm/m. The subset size was about 29 pixels, and the step size was 7 pixels. In this study, the loading angle of β was set to 0°, 30°, 60°, 90°, and three tests were carried out for each loading angle β.

3. Results

3.1 Strength and Failure Mode

Figure 6 shows the stress-strain curves of three specimens with β = 0°, 30°, 60°, 90°, and Fig. 7 shows the statistical results of strength of the specimens with respect to different β. The strength of the gneiss is greatly affected by loading angle of schistosity, and the variation of the strength with β exhibits approximately U-shaped distribution, which is similar to the results reported by others (Xu et al., 2018; Gholami and Rasouli, 2014). The strength is the smallest at β = 60°, and the ratio of average strength $\sigma_{c60°}/\sigma_{c0°}$ is about 0.48, indicating that the gneiss presents remarkable anisotropic characteristics. The change of strength with loading angle is mainly attributed to the change of failure mode. In general, the strength of layered rock is lower when shear failure occurs along the schistosity. Fig. 8 shows the typical failure modes with respect to different β. It can be seen that specimens with β = 0° and 30° exhibit mixed tensile-shear failure characteristics. At β = 0°, the primary cracks cut through rock matrix, and the crack extension path is tortuous. At β = 30°, the primary crack cuts across the matrix and locally shears along the schistosity. The

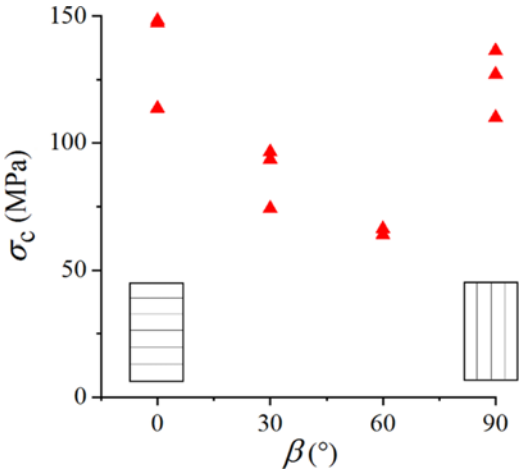

Fig. 7. Relationship between the Strength and the Loading Angle β

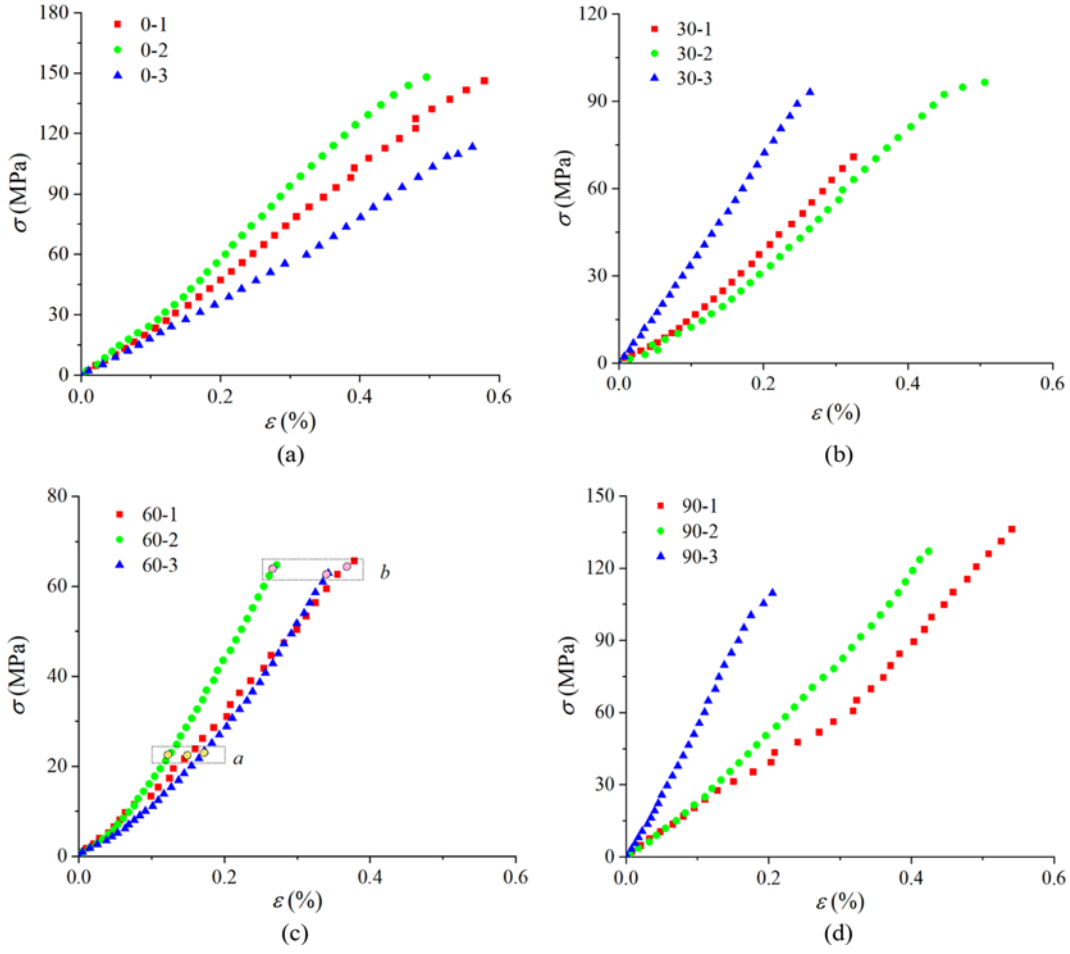

Fig. 6. Stress-Strain Curves of Three Specimens with Different β: (a) β = 0°, (b) β = 30°, (c) β = 60°, (d) β = 90°

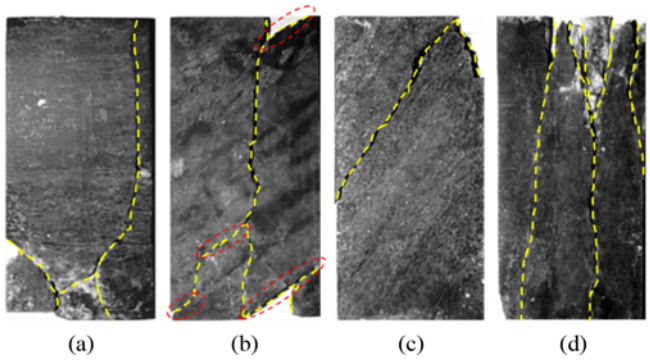

Fig. 8. Typical Failure Photographs of the Specimens with Different β: (a) $\beta = 0°$, (b) $\beta = 30°$, (c) $\beta = 60°$, (d) $\beta = 90°$

crack in the shearing section is relatively straight while the tension section is serrated. In this case, the failure of the specimen is controlled by both the rock matrix and the schistosity, and the primary shearing crack is completely developed along the schistosity. At $\beta = 60°$, the failure of shearing along the schistosity occurs. In this case, the failure is controlled by the schistosity only and the strength is relatively low. At $\beta = 90°$, the failure of splitting along the schistosity occurs, which is similar to the instability of the compression bar. Several macro cracks penetrate the specimen, forming several long strip slabs. This is mainly caused by the low tensile strength of the schistosity. The schistosity cracks under the action of lateral tensile strain. In this case, the failure of the specimen is controlled by the schistosity. The test results show that the strength and macroscopic failure mode of the gneiss are greatly affected by the loading angle β, showing strong anisotropy. This anisotropy is essentially due to the existence of flake minerals. These flake minerals, especially mica minerals, have low tensile and shear strengths. When the angle between the loading direction and the flaky minerals is small, it is easy to fracture along the cleavage of flaky minerals, and the micro fracture surface is relatively flat (Fig. 9(a)). In this case, the strength of the specimen is relatively low. When the angle is large, the fracture occurs through the hard minerals, such as quartz, and the micro fracture surface is rough with a lot of debris particles (Fig. 9(b)). Consequently, the strength is relatively high in this case.

3.2 Evolution Characteristics of Full-Field Strain with respect to Different Loading Angles

The full-field strain types can be divided into tensile strain, shear

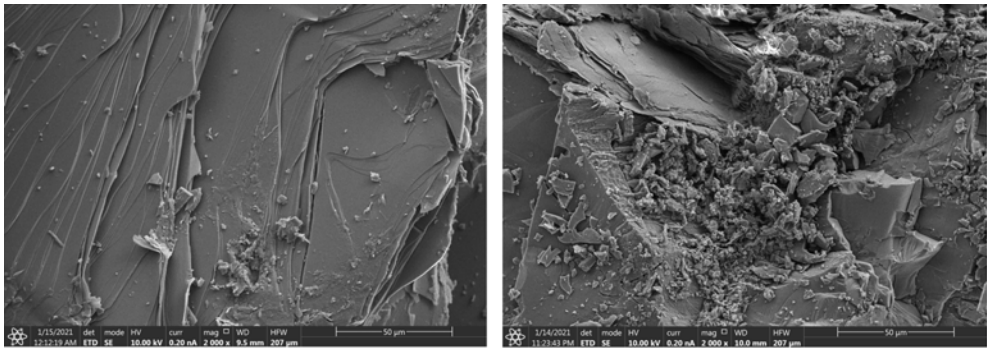

Fig. 9. Micromorphology (SEM) of the Fracture Plane: (a) Fracture along the Cleavage of Flaky Minerals, (b) Fracture through the Hard Minerals (SEM magnification 2000 × in each sub-figure)

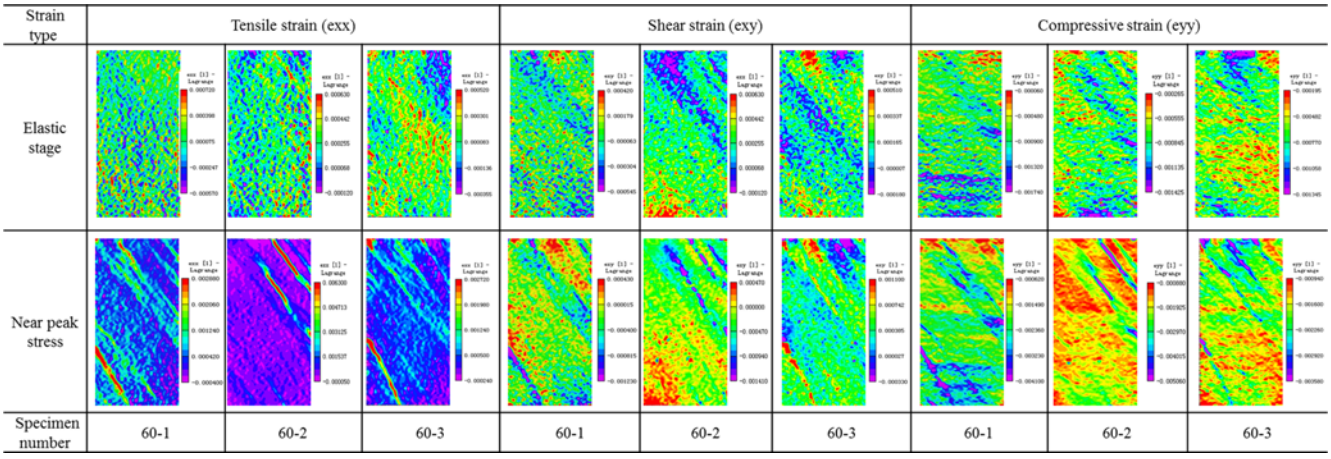

Fig. 10. Full-Field Strain (including tensile strain, shear strain, compressive strain) of Three Specimens with $\beta = 60°$ in Elastic Stage and Near Peak Stress

strain and compressive strain, and these strain types can be identified by VIC-2D software. The three specimens of $\beta = 60°$ are taken as examples, and the three strain types corresponding to different loading stages are extracted, which include the elastic stage (Section a in Fig. 6, about 40% of the peak stress), and near peak stress stage (Section b in Fig. 6). It can be seen from Fig. 10 that the full-field strain images of the three specimens in the same strain type are similar. For the tensile strain field, there is no obvious strain concentration zone in the elastic stage, but significant strain concentration zones appear near the peak stress stage. The strain concentration zones correspond well with the final fractures. For the shear strain field and compressive strain field, the strain concentration zones roughly along the schistosity in both elastic stage and near peak stress stage, but these zones are relatively dispersed and the strain magnitudes in the concentration area are lower than tensile strain. Among the three types of strain field images, the tensile strain field is more intuitive for progressive failure process analysis. Therefore, the information of tensile strain field of specimens with different loading angles is extracted. Because the variance of the strain field can reflect the non-uniform evolution process of the strain field, and the non-uniform evolution of the strain field is closely related to the development and propagation of micro cracks in the specimen (Ma et al., 2006). Therefore, the variance of tensile strain field is calculated and normalized (as shown in Eqs. (1) and (2) to reflect the evolution process of progressive failure):

$$S_{\varepsilon xx}(t) = \frac{\sum_{i=1}^{n}(x_i - \bar{x})^2}{n}, \tag{1}$$

$$v_{\varepsilon xx}(t) = \frac{S_{\varepsilon xx}(t)}{S_{\varepsilon xx}(t_{\max})}, \tag{2}$$

where $S_{\varepsilon xx}(t)$ is the variance of the full-field strain at a certain time, x_i is the tensile strain value at a specific point in the strain field, $\bar{x}$ is the average tensile strain value of all points in the strain field, $v_{\varepsilon xx}(t)$ is the normalized variance of the full-field strain at a certain time, and $S_{\varepsilon xx}(t_{max})$ is the variance of the full-field strain at the peak stress.

Figure 11 shows the variation of tensile strain variance ($v_{\varepsilon xx}$) and stress with loading time when β = 0°, 30°, 60°, 90°. As shown in Fig. 11, five typical stages can be roughly divided: (a) compaction stage (about 10% – 20% of the peak stress), (b) elastic stage (about 30% – 40% of the peak stress), (c) inflection stage of variance, (d) strain localization development stage and (e) near peak stress stage, and the corresponding strain field nephogram are extracted, as shown in Fig. 12, which are considered that these stages can reflect the progressive failure process.

It can be seen from Fig. 12 that at $\beta = 0°$, a concentrated strain strip is first formed at a weak schistosity plane, and then a tensile micro-crack initiates from the strip near the inflection stage of

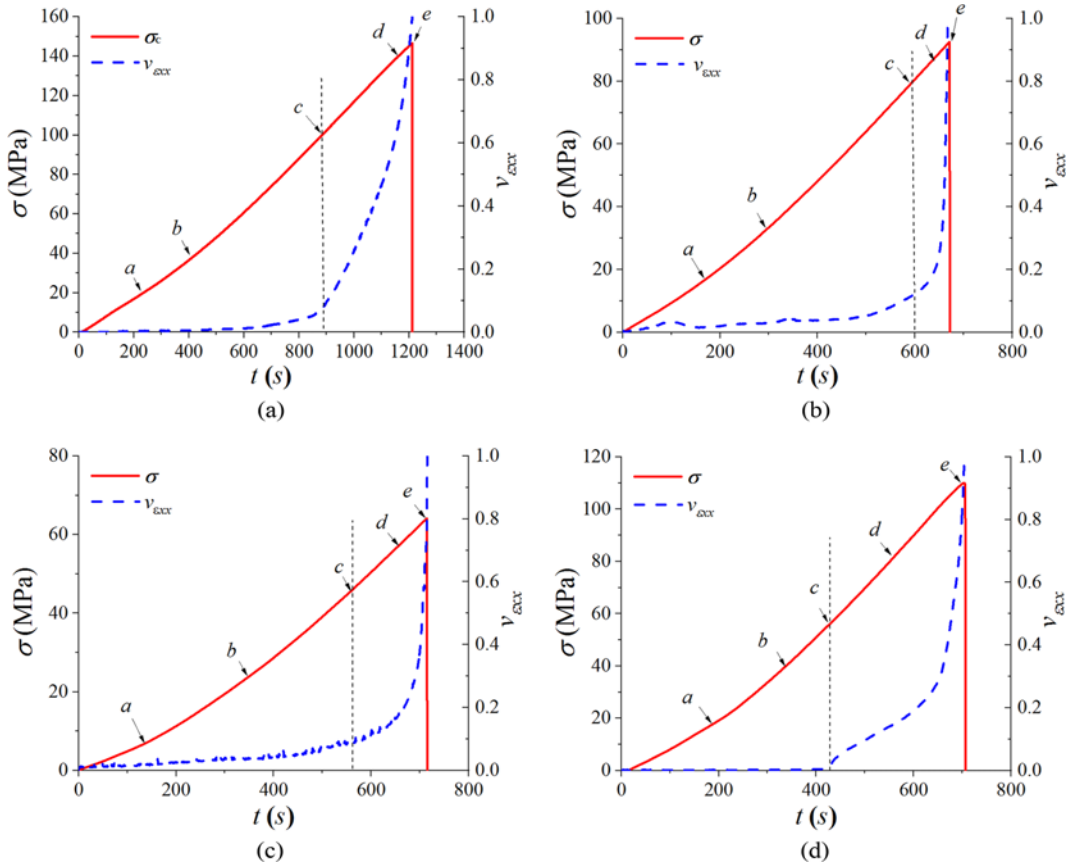

Fig. 11. Variation of Tensile Strain Variance ($v_{\varepsilon xx}$) and Stress with Loading Time: (a) $\beta = 0°$, (b) $\beta = 30°$, (c) $\beta = 60°$, (d) $\beta = 90°$

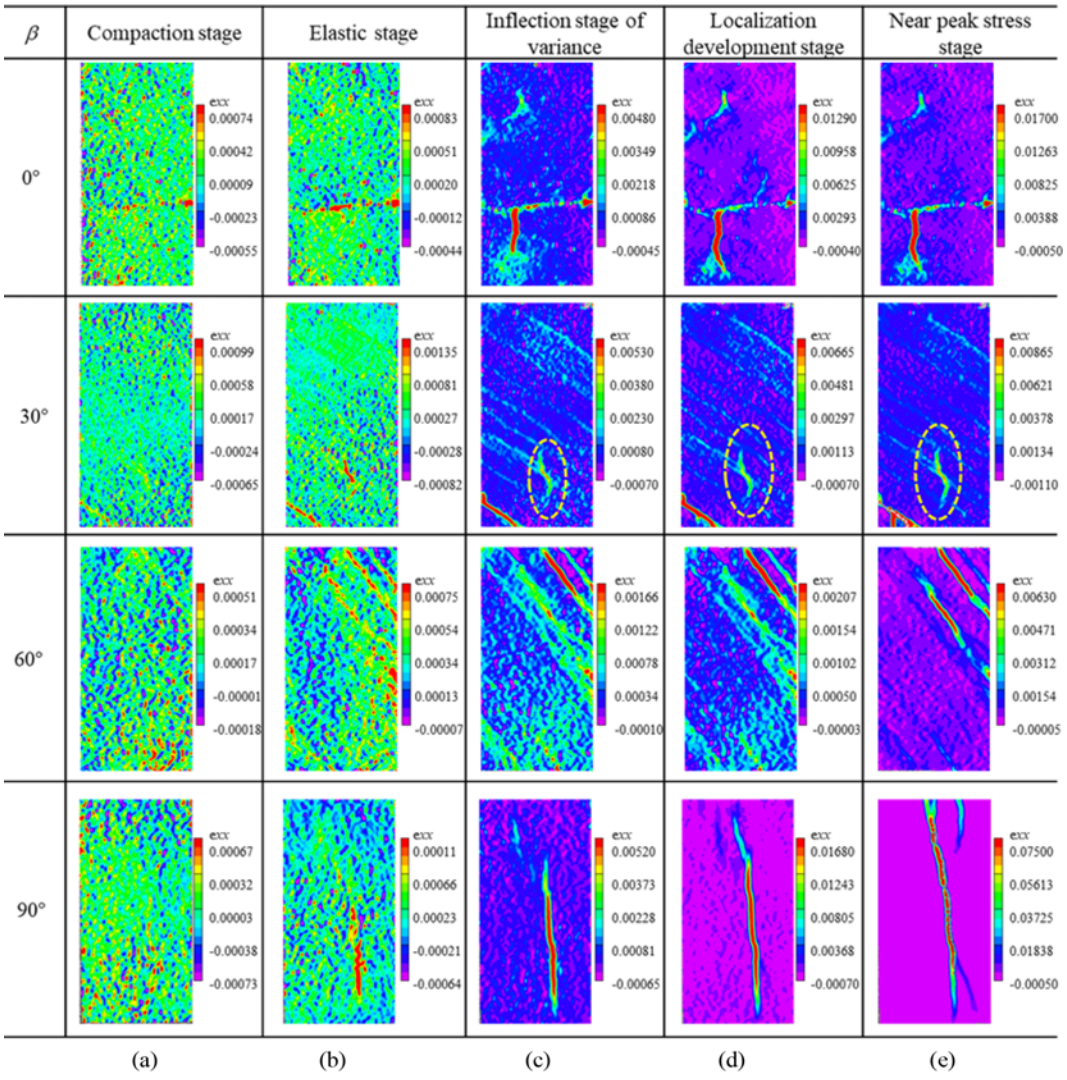

Fig. 12. Tensile Strain Field Nephogram of Five Stages: (a) Compaction Stage, (b) Elastic Stage, (c) Inflection Stage of Variance, (d) Localization Development Stage, (e) Near Peak Stress Stage

variance. The tensile micro-crack has no obvious propagation until the final failure. Similarly, the results of the other two specimens show analogous evolution characteristics. It can be inferred that the failure process of $\beta = 0°$ is mainly affected by the schistosity and microstructure. Due to the inhomogeneity of mineral composition and internal structure, tensile or shear micro-cracks mainly initiate from the microstructure, such as coarse-grained minerals, cleavage and micro-pore. Because of the directional arrangement of muscovite minerals, it is difficult for the micro-cracks to extend through the schistosity. The strain value of these high strain strips are further increasing with loading. Finally, the critical damage state is reached accompanying the rapid coalescing of micro-cracks and sudden mixed tensile-shear failure. The instantaneous energy release rate at the moment of failure is relatively high, accompanied by severe rock fragment ejection.

At $\beta = 30°$, the evolution of strain field is a transition between the cases $\beta = 0°$ and $\beta = 60°$. Similar to $\beta = 60°$, there are several strain strips developed along the schistosity direction. Because of the relatively small dip angle, the shear stress along the direction of schistosity is limited. When local shear slip occurs along mica minerals in the direction of schistosity, the existence of felsic minerals hinders the further development of microcracks, and then shear-induced tension crack is formed (as shown in the dotted circle in Fig. 12). During the subsequent loading process, the crack propagates slowly in a wing shape. Due to the limited shooting rate of the camera, the crack propagation path during the instantaneous failure of the specimen can't be captured, however, it can be inferred that the ultimate failure is caused by mixed tension-shear action from the final failure morphology of the specimen, as shown in Fig. 8(b). The failure mechanism is that the action of the tensile crack extending changes the local stress state, resulting in the activation of shearing along schistosity. Finally, the specimen lost its bearing capacity under the action of several non-coplanar shear cracks, (as shown in the dotted circle in Fig. 8(b). The tension crack cuts through rock matrix in a very

short time, indicating that the instantaneous energy release rate is high.

Compared with $\beta = 30°$, the shear stress required for failure along the schistosity is relatively lower at $\beta = 60°$. During the loading process, several high-strain strips are initiated which are potential failure planes. Because the shear strength of each schistosity plane is different, the ultimate failure is the result of the competition between these high-strain strips under the action of local stress field at this loading angle.

At $\beta = 90°$, the initiation and development of high-strain strip is relatively gradual. At the initial stage, the nephogram of tensile strain field is relatively uniform, and there is no obvious strain concentration zone. With further loading, the strain field begins to become non-uniform. In the elastic stage, the high-strain strip along the direction of schistosity can be identified, but the strain level is still relatively low and the spots are scattered. Because of the inhomogeneity of mineral composition and microstructure, the high-strain strip deflects during the propagation process, but the direction is generally parallel to the schistosity. The strip further extends and nearly penetrates the specimen at the localization development stage, however, this doesn't lead to immediate failure. The apparent deformation is mainly concentrated in the strain localized zone, and the micro-crack is almost open in essence, which splits the specimen into two nearly independent slabs, and ultimately the slab buckling and instability occurs. The maximum strain within the localization zone is 0.075 at the onset of failure, which is much larger than 0.0027 in the case of $\beta = 60°$. The result shows that the strain threshold is higher for tension along schistosity compared with shearing along schistosity at failure. From the above analysis, it can be concluded that the strain field evolution characteristics of specimens with different loading angles are quite different, and the development process of strain localization is closely related to the schistosity orientation and stress level.

3.3 Displacement Evolution Characteristics of Strain Localized Zones

When $\beta = 0°$ and $\beta = 30°$, the tensile-shear mixed failure through schistosity occurs easily. Before failure the process of crack propagation and coalescence is very rapid and it is difficult to identify the visible high-strain strip resulting in the ultimate failure. Therefore, it is also difficult to analyze the crack evolution quantitatively. When $\beta = 60°$ and $\beta = 90°$, tensile and shear failure occurs along the schistosity, which can be traced back to the strain localized zones resulting in failure. And the tension and shearing along the foliation are the typical failure modes of layered surrounding rock in situ, so the displacement evolution characteristics of strain localized zones in $\beta = 60°$ and $\beta = 90°$ cases are analyzed quantitatively. The displacement data extraction process is as follows: firstly, the strain localization strip resulting in the ultimate failure is selected; then, two points are selected symmetrically on both sides of the strain localization strip; next, the horizontal and vertical displacement components (u, v) of the two symmetrical points are extracted from the original data; next, the relative displacement components (Δu, Δv) are calculated, and

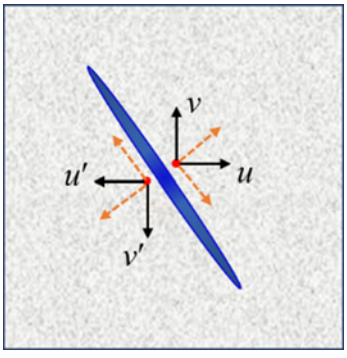

Fig. 13. Schematic Diagram of Displacement Data Processing on Both Sides of the Strain Localization Strip

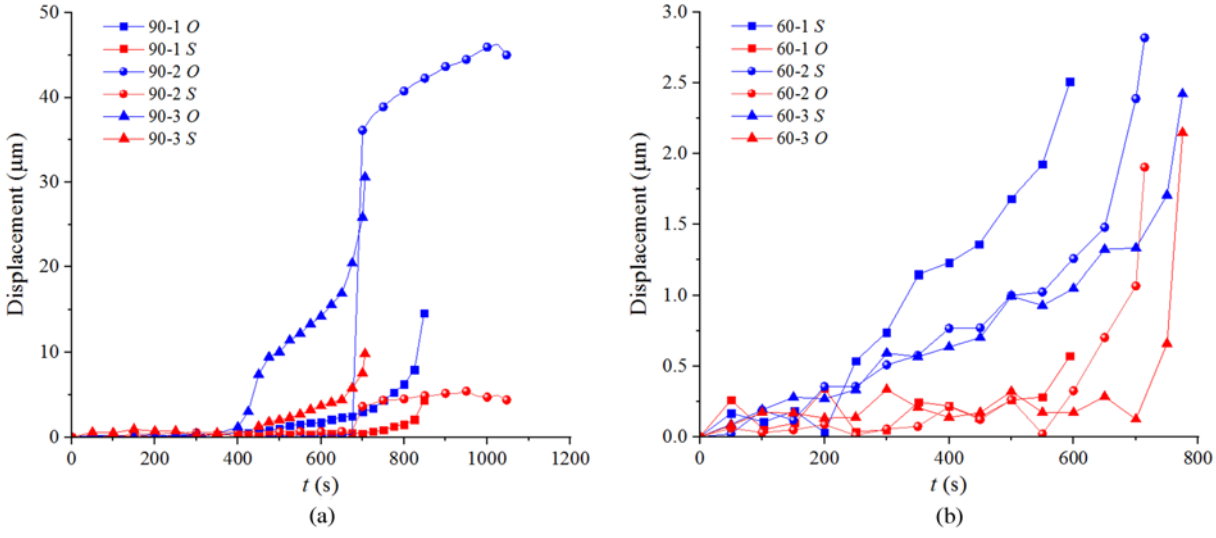

Fig. 14. Displacement Evolution Characteristics of Strain Localized Strip, which Includes Opening Component (O) and Slipping Component (S): (a) $\beta = 90°$, (b) $\beta = 60°$

then projected to the tangent direction and normal direction of the strip respectively (Fig. 13); finally, the slipping component (S) and opening component (O) of the strain localization strip are obtained, as shown in Eqs. (3) and (4):

$$S = \left|\Delta u \cdot \sin\beta + \Delta v \cdot \cos\beta\right|, \tag{3}$$

$$O = \left|\Delta u \cdot \cos\beta + \Delta v \cdot \sin\beta\right|. \tag{4}$$

Figure 14 shows the slipping component (S) and the opening component (O) of each group of the three specimens when β = 60° and β = 90°, respectively. It can be seen from Fig. 14 that at β = 90°, the opening displacement of the strain localization strip is much larger than the slipping displacement. In the early stages of loading, the displacement is approximately 0, and in the middle to late stages, the opening displacement increases suddenly, but the specimen doesn't lose stability immediately. Thereafter the opening displacement increases steadily until failure. At β = 60°, the displacement component of the strain localization strip is mainly slipping, and presents a stable increasing trend during the whole loading process. But the slipping displacement is far less in magnitude than the opening displacement in β = 90° case. From the above analysis, it can be concluded that the crack opening process is abrupt when tensile failure occurs along the schistosity (β = 90°), and the crack opening is relatively large before failure, however, the crack slip process is more stable when the shear failure occurs along the schistosity (β = 60°), and the crack slip is smaller before the failure. In general, during the loading process, the more energy is consumed in the crack propagation, the less energy is released when the specimen reaches the peak stress. Because the strain value in the strain localization strip of shearing along the schistosity is much less than that of tension along the schistosity, the energy release rate is higher and the failure is more violent at the stress peak.

3.4 Relationship between Principal Strain and Principal Stress

The deformation of layered rock mass is affected by both stress level and internal structure, and usually regarded as transversely isotropic body. The principal stress and the corresponding principal strain of a transversely isotropic elastic body are not coaxial

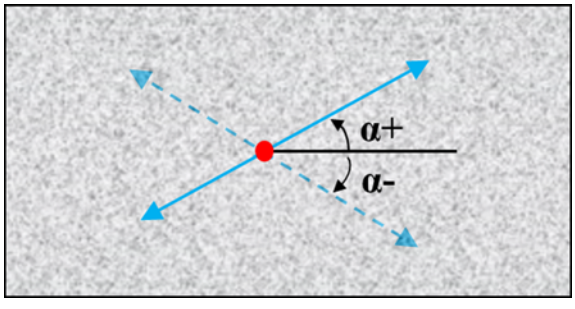

Fig. 15. Definition of Positive and Negative α: The Counterclockwise Rotation in the Horizontal Direction Is Defined as the Positive Angle (α+), and the Clockwise Rotation in the Horizontal Direction Is Defined as the Negative Angle (α-)

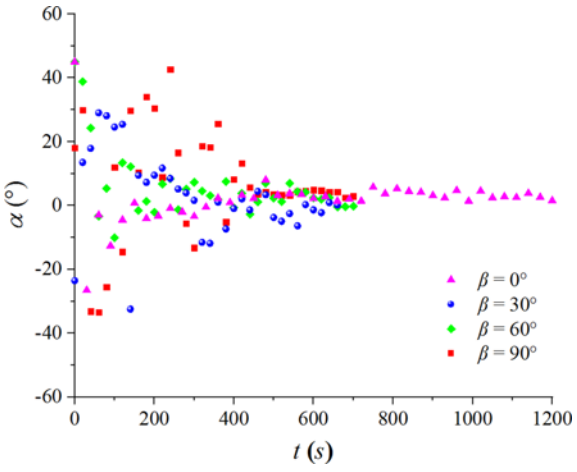

Fig. 16. Variation Characteristics of the Principal Tensile Strain Angle α during the Loading Process with respect to Different β

theoretically (Amadei, 1996). In order to understand the relationship between the principal strain and the principal stress of the specimen during the loading process, we assume that the principal compressive stress is always parallel to the longer side of the specimen during the loading process, and the deviation between the principal strain and the principal stress can be characterized by the angle α between the principal tensile strain and the horizontal direction. As shown in Fig. 15, the angle α formed by the counterclockwise rotation in the horizontal direction is defined as the positive angle (α+), and the angle α formed by the clockwise rotation in the horizontal direction is defined as the negative angle (α-). The calculation formula of α is shown in Eq. (5):

$$\alpha = \frac{1}{2}\arctan\frac{\gamma_{xy}}{2\left(\varepsilon_{xx} - \varepsilon_{yy}\right)}, \tag{5}$$

where γ_{xy} is the shear strain, ε_{xx} is the horizontal tensile strain, ε_{yy} is the vertical compressive strain.

The center position of the specimens shown in Fig. 12 is selected to calculate the angle α in order to minimize the influence of the end effect on the results. As shown in Fig. 16, the variation trend of non-coaxiality between principal strain and principal stress of specimens with different β is similar. At the initial stage of loading, the angle α fluctuates with loading process, which is probably caused by the void compaction or orientation adjustment of the microstructure such as flaky mineral and micropore. During the subsequent loading process, the variation of α is gradually stable and tends to zero. Therefore, no matter what the β is, the principal strain axis gradually approaches the corresponding principal stress axis in the loading process. It shows that the principal strain direction is affected by both the stress level and the inherent anisotropy, and the former is more significant near the peak strength.

4. Discussion

The evolution process of strain field of the foliated gneiss is

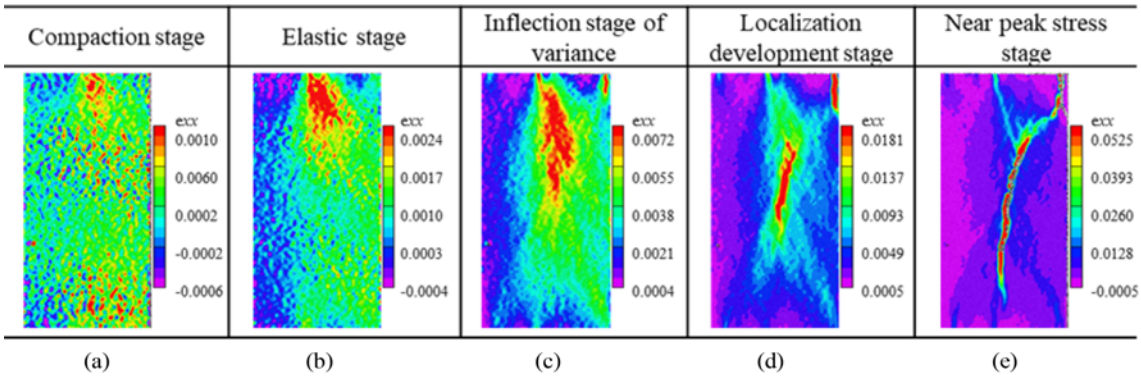

Fig. 17. Tensile Strain Field Nephogram of Five Stages for Marble: (a) Compaction Stage, (b) Elastic Stage, (c) Inflection Stage of Variance, (d) Localization Development Stage, (e) Near Peak Stress Stage

closely related to schistosity orientation and stress level. Moreover, the strain concentration strip appeared in the early stage of elastic loading and developed to a great extent near the inflection point of the variance curve. The progressive failure process of gneiss is quite different from that of isotropic rocks without layered structure. Fig. 17 shows the evolution nephogram of tensile strain field of marble with good homogeneity under the same loading condition. During the process of continuous loading, marble will produce a large range of material damage. When the damage accumulates to a certain extent, it will lead to structural deterioration, so that the specimen is no longer a complete material. The strain localization evolution of marble is quite different from gneiss. Affected by the internal structure, there is no continuous large-scale strain concentration area in the strain field evolution process of gneiss with different loading angles.

In the study of progressive failure process of rock, the characteristic stresses, such as crack initiation stress and damage stress, are usually identified by the information of deformation. The deformation are commonly measured by the strain gauge and displacement sensor in laboratory test. For the strain gauge, it usually measures the deformation within a small area on the surface of the specimen. Due to the strong heterogeneity of rocks, especially for layered rocks, the local deformation is usually distributed non-uniformly, as shown in Fig. 12. Therefore, the strain gauge is not suitable for identifying the progressive failure process of rock specimens. For the displacement sensor which can measure the overall deformation of the specimen, various methods were adopted, such as lateral deformation feedback and crack volume deformation method, to identify the characteristic stress in the progressive failure process of the specimen (Hoek and Martin, 2014). Since the characteristic stresses reflect the starting point of initiation and propagation of microcracks inside the specimen, these identification methods are essentially indirect methods based on macroscopic deformation information. On the other hand, the digital speckle correlation method can monitor the development of the strain concentration zones (mostly the microcrack development zones) of the specimen in real time, it can directly reflect the progressive failure process. However, it can be seen from Figs. 12 and 17 that the development of strain concentration zone is a gradual process, and it is difficult to identify the specific value of characteristic stresses, especially the crack initiation stress by DSCM only. From Fig. 12, it can be inferred that the stress levels of crack initiation are different for the gneiss with different β. The larger the β is, the lower the crack initiation stress is. For the damage stress, it can be roughly identified from the variance curve of the full-field strain. After the inflection of the variance curve, the non-uniformity of the full-field strain increases rapidly, indicating that internal microcracks are connected and coalesced, which can be regarded as the starting point of unstable crack propagation corresponding to the damage stress level.

5. Conclusions

In this paper, the progressive failure process and full-field strain evolution of an anisotropic gneiss with different loading angles are investigated by DSCM. The main conclusions can be drawn as follows:

1. The evolution process of the full-field tensile strain of the gneiss is closely related to schistosity orientation and stress level. More specifically, at $\beta = 0°$, the strain concentration zone mainly originates from the microstructure. The instantaneous energy release rate at the moment of final fracture is relatively high, accompanied by severe rock fragment ejection, and no potential fracture plane can be observed before failure; at $\beta = 30°$ and 60°, there are several strain concentration strips before failure, and the ultimate fracture is due to the competition of these high strain strips under the action of local stress field; at $\beta = 90°$, the initiation and propagation process of the strain concentration strip is asymptotically stable, and the strain threshold at the final fracture is higher.
2. When tensile failure occurs along the schistosity, the opening displacement of the strain localization band increases in a sudden manner during loading, but it does not lead to immediate failure. When the shear failure occurs along the schistosity, the displacement evolution of the strain localization band is mainly slip, and presents a gently stable growth

trend during loading, however, compared with the opening displacement for tensile failure along schistosity, the slip displacement is very small.

3. The principal strain axes gradually approach the corresponding principal stress axes during the loading process for different β. The principal strain direction is affected by both the stress level and the inherent anisotropy, and the former is more significant near the peak strength.
4. The progressive deformation and failure process of gneiss is quite different from that of isotropic rock without layered structure. Affected by the internal structure, there is no continuous large-scale strain concentration zone during the strain field evolution process for the gneiss with different loading angles.
5. From the full-field strain evolution, it can be inferred that the larger the β is, the smaller the crack initiation stress is. The damage stress can be roughly identified from the inflection of variance curve of full-field strain.

Acknowledgments

This study was financially supported by Chinese Natural Science Foundation with the Grant Nos 52079027, 51709043. The authors also thank Chun Wang, and Wen-Can Zhang at Northeastern University, China, for their assistance in specimen preparation and testing.

ORCID

Not Applicable

References

Amadei B (1996) Importance of anisotropy when estimating and measuring in situ stresses in rock. *International Journal of Rock Mechanics & Mining Sciences & Geomechanics Abstracts* 33(3): 293-325, DOI: 10.1016/s0148-9062(97)87420-7

Areias P, Reinoso J, Camanho PP, César de Sá J, Rabczuk T (2018) Effective 2D and 3D crack propagation with local mesh refinement and the screened poisson equation. *Engineering Fracture Mechanics* 189:339-360, DOI: 10.1016/j.engfracmech.2017.11.017

Chen JX, Liu WW, Chen LJ, Luo YB, Li Y, Gao HJ, Zhong DC (2020) Failure mechanisms and modes of tunnels in monoclinic and soft-hard interbedded rocks: A case study. *KSCE Journal of Civil Engineering* 24(4):1357-1373, DOI: 10.1007/s12205-020-1324-3

Chenevert ME, Gatlin C (1965) Mechanical anisotropies of laminated sedimentary rocks. *Society of Petroleum Engineers Journal* 5(01): 67-77, DOI: 10.2118/890-PA

Dautriat J, Bornert M, Gland N, Dimanov A, Raphanel J (2011) Localized deformation induced by heterogeneities in porous carbonate analysed by multi-scale digital image correlation. *Tectonophysics* 503(1-2): 100-116, DOI: 10.1016/j.tecto.2010.09.025

Donath FA (1961) Experimental study of shear failure in anisotropic rocks. *Geological Society of America Bulletin* 72(6):985-989, DOI: 10.1130/0016-7606(1961)72[985:ESOSFI]2.0.CO;2

Gholami R, Rasouli V (2014) Mechanical and elastic properties of transversely isotropic slate. *Rock Mechanics and Rock Engineering* 47(5):1763-1773, DOI: 10.1007/s00603-013-0488-2

Heng S, Guo YT, Yang CH, Daemen JJ, Li Z (2015) Experimental and theoretical study of the anisotropic properties of shale. *International Journal of Rock Mechanics & Mining Sciences* 74:58-68, DOI: 10.1016/j.ijrmms.2015.01.003

Hoek E, Martin CD (2014) Fracture initiation and propagation in intact rock — A review. *Journal of Rock Mechanics and Geotechnical Engineering* 6(4):287-300, DOI: 10.1016/j.jrmge.2014.06.001

Jaeger JC (1960) Shear failure of anisotropic rocks. *Geological Magazine* 97(1):65-72, DOI: 10.1017/S0016756800061100

Li A, Shao GJ, Su JB, Sun Y, Yu TT, Shi HG (2018) Influence of heterogeneity on mechanical and acoustic emission behaviours of stratified rock specimens. *European Journal of Environmental and Civil Engineering* 22:381-414, DOI: 10.1080/19648189.2017.1373709

Ma SP, Wang LG, Jin GC (2006) Damage evolution inspection of rock using digital speckle correlation method (DSCM). *Key Engineering Materials* 326-328(Pt2):1117-1120, DOI: 10.4028/www.scientific.net/KEM.326-328.1117

Mogi K (2006) Experimental rock mechanics. Taylor and Francis, London, UK, 10-15

Nasseri MHB, Rao KS, Ramamurthy T (2003) Anisotropic strength and deformation behavior of himalayan schists. *International Journal of Rock Mechanics and Mining Sciences* 40(1):3-23, DOI: 10.1016/S1365-1609(02)00103-X

Nicksiar M, Martin CD (2012) Evaluation of methods for determining crack initiation in compression tests on low-porosity rocks. *Rock Mechanics and Rock Engineering* 45(4):607-617, DOI: 10.1007/s00603-012-0221-6

Pan B, Qian K, Xie H, Asundi A (2009) Two-dimensional digital image correlation for in-plane displacement and strain measurement: A review. *Measurement Science & Technology* 20(6):152-154, DOI: 10.1088/0957-0233/20/6/062001

Pan PZ, Yan F, Feng XT, Wu ZH, Qiu SL (2019) Modeling of an excavation-induced rock fracturing process from continuity to discontinuity. *Engineering Analysis with Boundary Elements* 106(9): 286-299, DOI: 10.1016/j.enganabound.2019.05.014

Rabczuk T, Belytschko T (2004) Cracking particles: A simplified meshfree method for arbitrary evolving cracks. *International Journal for Numerical Methods in Engineering* 61(13):2316-2343, DOI: 10.1002/nme.1151

Rabczuk T, Belytschko T (2007) A three-dimensional large deformation meshfree method for arbitrary evolving cracks. *Computer Methods in Applied Mechanics and Engineering* 196(29-30):2777-2799, DOI: 10.1016/j.cma.2006.06.020

Ren HL, Zhuang XY, Anitescu C, Rabczuk T (2019) An explicit phase field method for brittle dynamic fracture. *Computers & Structures* 217(6):45-56, DOI: 10.1016/j.compstruc.2019.03.005

Song H, Zhang H, Fu D, Kang Y, Huang G, Qu C (2013) Experimental study on damage evolution of rock under uniform and concentrated loading conditions using digital image correlation. *Fatigue & Fracture of Engineering Materials & Structures* 36(8):760-768, DOI: 10.1111/ffe.12043

Xiong LX, Li TB, Yang LD (2014) Biaxial compression creep test on green-schist considering the effects of water content and anisotropy. *KSCE Journal of Civil Engineering* 18(1):103-112, DOI: 10.1007/s12205-014-0276-x

Xu GW, He C, Su A, Chen ZQ (2018) Experimental investigation of the anisotropic mechanical behavior of phyllite under triaxial compression. *International Journal of Rock Mechanics and Mining Sciences* 104:

100-112, DOI: 10.1016/j.ijrmms.2018.02.017

Xu NW, Li TB, Dai F, Li B, Zhu YG, Yang DS (2015) Microseismic monitoring and stability evaluation for the large scale underground caverns at the Houziyan hydropower station in southwest china. *Engineering Geology* 188:48-67, DOI: 10.1016/j.enggeo.2015.01.020

Yang G, Cai Z, Zhang X, Fu D (2015) An experimental investigation on the damage of granite under uniaxial tension by using a digital image correlation method. *Optics and Lasers in Engineering* 73:46-52, DOI: 10.1016/j.optlaseng.2015.04.004

Yin PF, Yang SQ, Tian WL, Cheng JL (2019) Discrete element simulation on failure mechanical behavior of transversely isotropic rocks under different confining pressures. *Arabian Journal of Geosciences* 12(19):1-21, DOI: 10.1007/s12517-019-4807-0

Zhang XP, Wong LNY, Wang SJ, Han GY (2011) Engineering properties of quartz mica schist. *Engineering Geology* 121:135-149, DOI: 10.1016/j.enggeo.2011.04.020